

β -NaMnO₂: a High Performance Cathode for Sodium-Ion Batteries

Juliette Billaud,[†] Raphaële J. Clément,[‡] A. Robert Armstrong,[†] Jesús Canales-Vázquez,[§] Patrick Rozier,[⊥] Clare P. Grey[‡] and Peter G. Bruce^{◇*}

[†] School of Chemistry, University of St. Andrews, St. Andrews, Fife, KY16 9ST, UK

[‡] Department of Chemistry, Lensfield Road, Cambridge, CB2 1EW, UK

[§] Renewable Energy Research Institute, University of Castilla-La Mancha, 02071 Albacete, Spain

[⊥] Institut Carnot CIRIMAT, CNRS UMR 5085, Université Paul Sabatier, Toulouse III, France

[◇] Departments of Materials and Chemistry, University of Oxford, UK

KEYWORDS. Sodium-Ion Battery, High performance, Rate capability, Solid-State NMR

ABSTRACT: There is much interest in Na-ion batteries for grid storage because of the lower projected cost compared with Li-ion. Identifying Earth abundant, low cost and safe materials that can function as intercalation cathodes in Na-ion batteries is an important challenge facing the field. Here we investigate such a material, β -NaMnO₂, with a different structure from that of NaMnO₂ polymorphs and other compounds studied extensively in the past. It exhibits a high capacity (of ca. 190 mA h g⁻¹ at a rate of C/20), along with a good rate capability (142 mA h g⁻¹ at a rate of 2C) and a good capacity retention (100 mA h g⁻¹ after 100 Na extraction/insertion cycles at a rate of 2C). Powder XRD, HRTEM and ²³Na NMR studies revealed that this compound exhibits a complex structure consisting of intergrown regions of α -NaMnO₂ and β -NaMnO₂ domains. The collapse of the long-range structure at low Na content is expected to compromise the reversibility of the Na extraction and insertion processes occurring upon charge and discharge of the cathode material, respectively. Yet stable, reproducible and reversible Na intercalation is observed.

1. INTRODUCTION

The renaissance of interest in sodium-based rechargeable batteries has been driven by the greater and more uniform Earth abundance of sodium, compared with lithium, and hence potentially lower cost.¹⁻⁶ The larger mass of Na, compared with that of Li, leads to a lower specific capacity for sodium cells, with respect to equivalent lithium cells, but this is no disadvantage for static applications such as the storage of electricity on the grid. It is the possibility of discovering sodium intercalation (insertion) compounds that might outperform lithium intercalation compounds, leading to a new generation of sodium-based rechargeable batteries, that is perhaps the most significant motivation for the investigation of sodium intercalation materials.

Potential sodium intercalation cathodes, such as 3D framework compounds, especially those based on the NASICON structure, have received considerable attention because of the high Na⁺ conductivity of the solid electrolyte, Na₃Zr₂Si₂PO₁₂, with a similar structure.^{1-3,7-10} The layered Li transition metal oxide LiCoO₂, and related materials have been the dominant cathodes for lithium-ion

cells.¹¹⁻¹⁶ Layered Na transition metal compounds, NaMO₂, exhibit extensive intercalation chemistry, more so than their Li counterparts. For example, both NaFeO₂ and NaCrO₂ are electrochemically active in contrast to their lithium analogues,^{17,18} and NaMnO₂ compounds can sustain sodium deintercalation without conversion to the spinel structure, unlike layered LiMnO₂.¹⁹⁻²¹

A number of recent studies on sodium intercalation compounds have focused on Earth abundant and hence low-cost transition metals, especially Mn and Fe. Of the layered Na_xMnO₂ compounds, α -NaMnO₂, which exhibits a monoclinic distortion of the O₃ crystal structure of LiCoO₂ (ABC oxygen stacking), and P2-Na_{0.67}MnO₂ (ABBA oxygen stacking), have been widely studied as sodium positive electrode materials.^{19,22-24} The reversibility of the deintercalation process in the P2 polymorph is enhanced by Mg doping.²⁵ Similarly, substitution of Mn by lithium in P2 Na_x[M_{1-y}Li_y]O₂ compounds leads to improved reversibility of the charge (that is, the electrochemical Na insertion) process.^{26,27} Solid solutions of Mn and Fe, Na_x[Mn_{1-y}Fe_y]O₂, adopting either O₃ or P2 structures, have also been investigated.^{28,29}

β -NaMnO₂ possesses a different layered structure from that conventionally adopted by NaMO₂ type structures. Instead of planar layers of MnO₆ octahedra that simply alter their stacking sequence to generate the different polymorphs (O₃, P₂, P₃, etc.),³⁰ β -NaMnO₂ is composed of zig-zag layers of edge sharing MnO₆ octahedra between which Na⁺ ions reside in octahedral sites, Figure 1.³¹

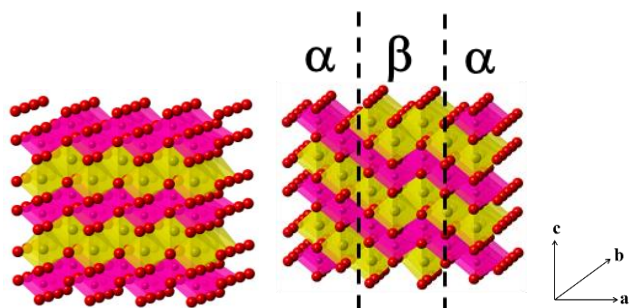


Figure 1. a) Schematic representation of β -NaMnO₂ in the $Pmnm$ space group and b) intergrowth model between α and β -NaMnO₂. MnO₆ octahedra are pink, NaO₆ octahedra are yellow and O atoms are red. Adapted from Abakumov *et al.*³⁴.

The structure possesses an orthorhombic symmetry, space group $Pmnm$, with cell parameters $a = 2.86$, $b = 4.79$, $c = 6.33$ Å. The c axis is perpendicular to the layers in this setting.³¹ Sodium deintercalation was first investigated by Mendiboure *et al.*, demonstrating reversible removal of 0.15 Na at a potential of around 2.7 V vs. Na⁺/Na.²² A phase formed upon electrochemical Na extraction from NaMnO₂ was identified with the same space group as the pristine (as-synthesized) phase, but with a significant reduction of the Jahn-Teller distortion, associated with Mn³⁺ to Mn⁴⁺ oxidation. Here we show that β -NaMnO₂ can exhibit a first discharge capacity (that is, the capacity to electrochemically reinsert Na in the material) as high as 190 mA h g⁻¹, corresponding to the removal of 0.82 Na per formula unit. A discharge capacity of ca. 130 mA h g⁻¹ is retained after 100 cycles.

2. EXPERIMENTAL METHODS

2.1. Synthetic procedures. The β -NaMnO₂ samples were prepared by solid-state synthesis. The solid-state route involved mixing together Na₂CO₃ and Mn₂O₃; 15% weight excess of sodium was used in order to compensate for Na₂O evaporation on firing. Two firing steps were necessary, firstly at 950 °C for 24 hours, after a temperature ramp of 1 °C/min, and secondly at 950 °C for 24 hours, after ramping the temperature at a faster heating rate of 5 °C/min. Both firing steps were performed on pellets under oxygen flow, and followed by a quench to room temperature. The samples were then transferred to an Ar-filled glovebox.

2.2. Powder X-ray diffraction. Powder X-ray diffraction (XRD) was performed on a Stoe STADI/P diffractometer operating in transmission mode with FeK α radiation

($\lambda = 1.936$ Å) and using a capillary to avoid contact with the air. The Diffax program was used to model the diffracted intensities.³²

2.3. In situ X-ray diffraction. *In situ* X-ray diffraction data were collected on a Bruker D8 diffractometer operating in Bragg-Brentano geometry with CuK α radiation ($\lambda = 1.5416$ Å). The set-up consisted of an *in situ* cell with an X-ray transparent Beryllium window (thickness of 200 μ m). In order to prevent Be oxidation at high potentials (above 3.8 V vs. Na⁺/Na), a protective Al foil (thickness 10 μ m) was placed between the Be window and the powder under study. The cell was connected to a Biologic cycler and the evolution of the potential was recorded as a function of the time.

2.4. Transmission Electron Microscopy. TEM was performed on a Jeol JEM 2100 electron microscope operating at 200 kV and equipped with a double-tilt ($\pm 25^\circ$) sample holder, an EDS detector (Oxford Link), and an Orius SC200 CCD Camera. TEM specimens were prepared by dispersing the oxides in dry hexane under an inert atmosphere, and depositing a few drops of the suspension on to a holey carbon-coated copper grid (EMS). TEM images were analyzed using the Digital Micrograph™ software from Gatan.

2.5. Electrode preparation. Composite electrodes were cast on aluminum foil in an Ar-filled glovebox to prevent air oxidation. The slurry was prepared by mixing β -NaMnO₂, super S carbon, and Kynar Flex 2801 as binder, in weight ratios of 75:18:7, in THF. Electrodes were incorporated into coin cells (CR2325 type) with a sodium metal counter electrode, and with an electrolyte solution composed of 1M NaPF₆ in ethylene carbonate : propylene carbonate : dimethyl carbonate, in weight ratios of 45:45:10, respectively. Typical electrode active material loadings were ca. 4-5 mg/cm². The electrode used for *in situ* powder X-ray measurements was prepared using the same composition as described above (up to 20 mg per cell), but in powder form. The samples for *ex situ* measurements (TEM, PXRD, and Na NMR) were prepared by extracting the cathode material from the coin cells and washing it with dry dimethyl carbonate (DMC). The solvent was then evaporated. All steps were performed in an Ar-filled glovebox. The resulting powder was stored in an Ar-filled glovebox for further characterization.

2.6. Electrochemical measurements. Electrochemical measurements were carried out at room temperature using a Maccor Series 4200 battery cycler.

2.7. Solid-state NMR. NMR experiments were performed under 60 kHz MAS, using a 1.3 mm double-resonance HX probe. ²³Na 1D spin echo spectra were recorded at room temperature on a Bruker Avance III 200 wide-bore spectrometer, at a Larmor frequency of -77.9 MHz, and ²³Na NMR chemical shifts were referenced against NaCl. ²³Na spin echo spectra were acquired using a 90° RF (radio frequency) pulse of 1 μ s at 25.04 W, a 180° pulse of 2 μ s at 25.04 W, and a recycle delay of 30 ms. ²³Na

RF pulses were assumed to be selective for the ^{23}Na central transition.

2.8. Chemical Analyses. Chemical analyses were performed by Inductively Coupled Plasma (ICP) emission spectroscopy.

3. RESULTS AND DISCUSSION

3.1. Electrochemistry. $\beta\text{-NaMnO}_2$ samples were synthesized, characterized and incorporated into electrochemical cells as described in the experimental section. Load curves (corresponding to electrochemical Na extraction and reinsertion) for $\beta\text{-NaMnO}_2$ are shown in Figure 2.

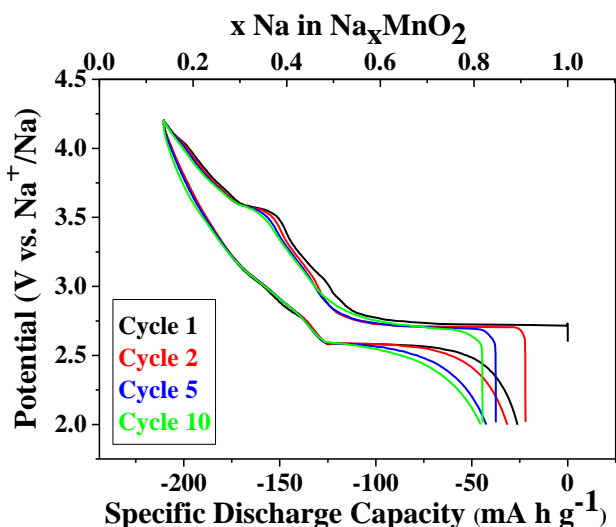


Figure 2. Load curves for $\beta\text{-NaMnO}_2$ at a rate of $C/20$ (10 mA g^{-1}). The 1st, 2nd, 5th and 10th Na extraction/reinsertion cycles are represented in black, red, blue and green, respectively.

The 200 mA h g^{-1} obtained on the first charge commences with an extended plateau between NaMnO_2 and a phase with a composition close to $\text{Na}_{0.57}\text{MnO}_2$, followed by a rising potential interrupted by small steps at $\text{Na}_{0.49}\text{MnO}_2$ and $\text{Na}_{0.39}\text{MnO}_2$. These steps are still present upon discharge, but are less pronounced, and the same extended voltage plateau is observed at the end of discharge. There is an irreversible loss of capacity corresponding to 25 mA h g^{-1} (equivalent to 0.1 Na per formula unit). The shapes of the load curves are almost invariant on cycling, and only exhibit a small but continuous reduction in capacity associated mainly with the voltage plateau. The 2.7 V plateau is associated with the phase transition between the Jahn-Teller distorted and undistorted structures and exhibits a small polarization (below 150 mV).

3.2. Structural characterization.

Structure of the as-prepared material

In order to understand the structural changes that accompany sodium deintercalation and reinsertion, the structure of $\beta\text{-Na}_x\text{MnO}_2$ was monitored by a combination of powder X-ray diffraction, solid state NMR and high-resolution transmission electron microscopy. The PXRD pattern of the as-prepared material is shown in Figure 3.

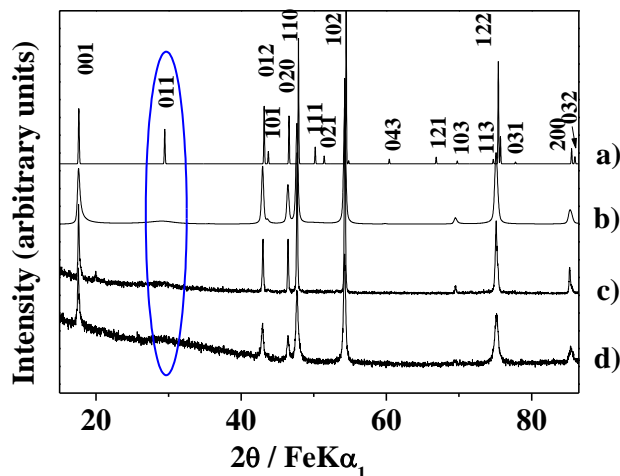


Figure 3. X-ray diffraction patterns of a) the ideal $\beta\text{-NaMnO}_2$ structure in the $Pmnm$ space group, b) simulated with 25 % stacking faults, c) as-prepared $\beta\text{-NaMnO}_2$ and d) after 5 cycles. Highlighted with the blue circle is the major difference between the ideal and experimental data with the (011) peak greatly broadened.

It is apparent from Figure 3 that the structure, although clearly based on that of $\beta\text{-NaMnO}_2$, cannot be described by the ideal structure for this compound, see for example the (011) peak in the region highlighted by the ellipse. Diffax has been used to simulate the effect of introducing random stacking faults corresponding to the insertion of a monoclinic $\alpha\text{-NaMnO}_2$ cell between two blocks of orthorhombic symmetry, as shown in Figure 1.³² Stacking faults are not uncommon in battery materials.^{33,34} Those observed here are similar to the microtwinning seen in the Ramsdellite form of MnO_2 , although in $\beta\text{-NaMnO}_2$ there is also a Jahn-Teller distortion.³⁴ The stacking faults in $\beta\text{-NaMnO}_2$ are most closely related to those in the isostructural and similarly Jahn-Teller distorted LiMnO_2 material, albeit in a lower proportion (1-7 % occurrence).³⁵ For $\beta\text{-NaMnO}_2$ the experimental powder diffraction pattern is well represented by a structural model composed of 25% stacking faults. Simulations using other proportions of stacking faults are shown in Figure S1. While the agreement between the experimental powder diffraction pattern and the simulation pattern with 25% stacking faults is compelling, and certainly demonstrates that this material cannot be described by a single structure, Diffax cannot reveal the detailed nature of the structural complexity. A recent in-depth HRTEM study of $\beta\text{-NaMnO}_2$ confirms that this material is composed of structural motifs built from the α and β crystal structures.³⁶ The two structures are energetically very similar and they can form a

low energy phase boundary (a twin plane), where the MnO_6 layers in the α and β phases are oriented at approximately 60° to each other, as indicated in Figure 1 b).³⁶ Intergrowth of blocks of the α and β - NaMnO_2 crystal structures of different sizes leads to various intermediate structures. Our own TEM data, coupled with NMR data, reinforce this recent interpretation, as shown in Figure S2 and in Figure 4. Our as-prepared material is composed of regions exhibiting an ideal β -like stacking sequence and regions in which twin planes between the α and β phases lead to stacking faults. Disorder along the c -axis is obvious from the TEM images of the pristine material, indicating some degree of disorder in the as-prepared compound.

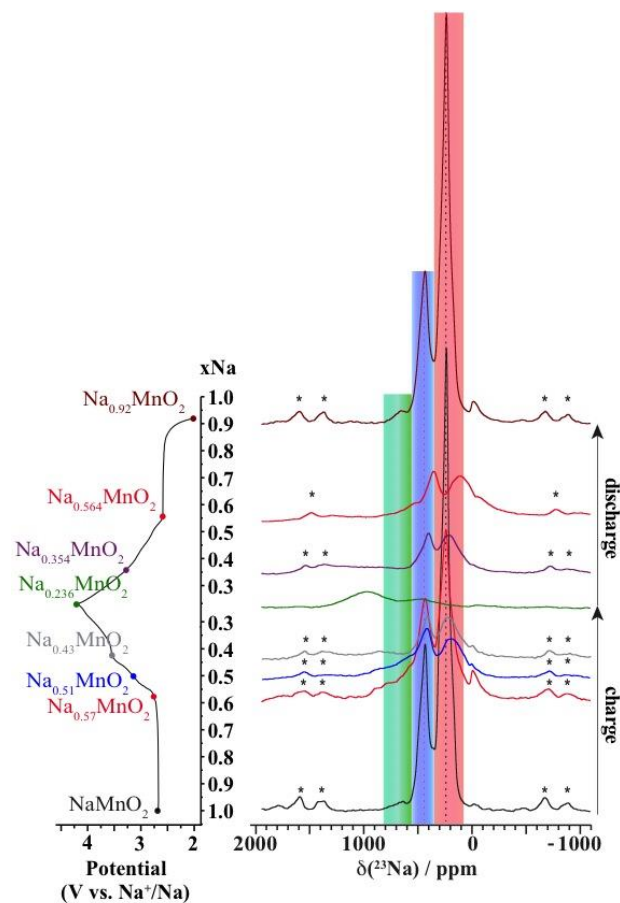


Figure 4. *Ex situ* ^{23}Na spin echo NMR spectra obtained at different stages of the first electrochemical cycle, under an external field of 200 MHz and at a spinning frequency of 60 kHz. Spinning sidebands are marked with an asterisk (*). The three regions containing the resonances of Na atoms in a pure α environment, in a pure β environment, and in the vicinity of a stacking fault are highlighted in green, red, and blue, respectively. These regions are not valid for the sample with lowest Na content ($\text{Na}_{0.236}\text{MnO}_2$), for which significant disorder in the crystal structure leads to broadening of the NMR peaks, and Mn^{3+} to Mn^{4+} oxidation induces a larger Fermi contact shift with all Na resonances being shifted towards the LHS of the spectrum. The peak near 0 ppm is due to Na^+ in a diamagnetic environment, most probably from resid-

ual electrolyte or its decomposition products formed during cycling.

The assignment of the two main peaks in the ^{23}Na NMR spectrum of the pristine phase (Figure 4) was assisted by a previous NMR study,³⁷ and by comparison to the ^{23}Na NMR spectrum collected on the α phase, presented in Figure S4. The presence of two ^{23}Na NMR resonances is consistent with a high proportion of defects, given that the structure of the ideal β structure only has one Na crystallographic site. A third, low intensity Na peak at *ca.* 650 ppm matches the Na resonance observed in the α polymorph, suggesting that there may be a minority of Na sites in regions of short-range α -like order in the pristine β phase.³⁷ This observation is in agreement with a previous experimental TEM and synchrotron powder XRD study on the β polymorph.³⁶ Integration of the spectrum reveals that the two major types of Na environments occur in an approximately 2 to 1 ratio. We assign the main Na resonance, occurring at 237 ppm, to Na in an ideal β -structure. The second peak has a shift of 433 ppm, intermediate between the ^{23}Na NMR shifts corresponding to the ideal α and β environments (at 656 ppm and 237 ppm, respectively), and is therefore assigned to a Na environment in the vicinity of a planar defect. Preliminary DFT calculations of the ^{23}Na NMR parameters on the α and β polymorphs support this assignment and will be presented in a future publication, along with a more detailed analysis of stacking fault formation in NaMnO_2 .

Structural changes on cycling

Given the considerable structural complexity of β - NaMnO_2 it is remarkable that the load curve remains relatively invariant on cycling (Figure 2). To investigate the structural changes in more detail *in situ* PXRD and *ex situ* NMR data were collected as a function of charge/discharge (that is, Na extraction and reinsertion) and are presented in Figures 4 and 5.

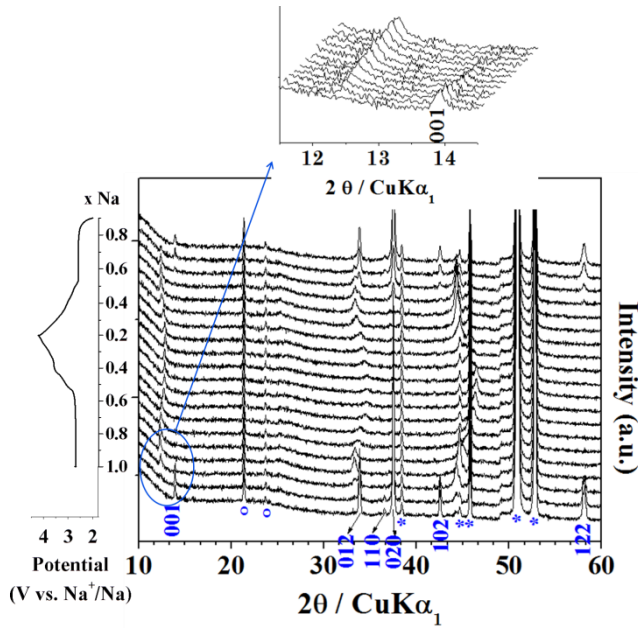


Figure 5. *In situ* powder X-ray diffraction patterns of β - NaMnO_2 recorded during the first electrochemical cycle at $C/10$ every 0.08 Na^+ exchanged. The region between 12 and 15° in 2θ is highlighted in order to show the gradual reduction in intensity of the (001) peak, and the gradual appearance of a peak at lower 2θ angles associated with the two phase deintercalation. The symbol * represents the Be window and the $^\circ$ symbol comes from other components of the *in situ* cell.

Both *in situ* PXRD and *ex situ* NMR data are presented with the unfolded load curve on the left hand side of the figure, the diffraction patterns and NMR spectra located at the correct positions on the charge/discharge curves. The diffraction patterns associated with the voltage plateaus at the beginning of the Na extraction process, and when Na is fully reinserted, are consistent with a mixture of two phases, with varying ratios but no compositional change, across the plateau. This is perhaps most evident in the expanded region in Figure 5 from 12 to 15° in 2θ ($\text{CuK}\alpha$), where the (001) peak of the β - NaMnO_2 structure diminishes in intensity, while the new peak at lower angles increases. The Na deficient phase with a composition close to $\text{Na}_{0.57}\text{MnO}_2$ can be assigned to a structure with the same $Pnmm$ space group but from which the Jahn-Teller distortion has been removed, leading to significantly different lattice parameters in close agreement with those reported by Mendiboure *et al.* for $\text{Na}_{0.91}\text{MnO}_2$.²² However, the overriding conclusion from the *in situ* powder X-ray diffraction data is that there is a major collapse of the long-range structure at low sodium content, with many of the peaks disappearing and those that remain exhibiting significant broadening in most cases. The loss of order is also evident from the TEM data acquired on the sample with the lowest Na content, with an average composition of $\text{Na}_{0.23}\text{MnO}_2$ in which the crystals develop a mosaic structure of domains, as shown in Figure S2. The significant structural disorder at the end of the Na extrac-

tion process may result from an increase in the proportion of stacking faults upon Na removal, as indicated in the NMR data.

The ^{23}Na NMR spectra collected at different Na compositions show that the relative intensities of the two major peaks decrease continuously when Na is extracted. The faster rate of decrease of the peak corresponding to the β environment, compared to the peak assigned to Na at the stacking faults, either indicates preferential extraction of sodium from the β - NaMnO_2 regions and/or may be related to the loss of long-range order observed in TEM and in XRD data: more planar defects are formed as Na is extracted, leading to fewer Na^+ in pure β environments and more Na^+ in stacking fault environments. At low Na content, the Na NMR peaks become broad, confirming a significant disorder in the material. As expected, an increase in the Na shifts is observed upon Na removal, as the oxidation of Mn^{3+} to Mn^{4+} leads to a higher hyperfine shift, the main contribution to the total Na shift in paramagnetic NaMnO_2 . A full analysis of the NMR of the different *ex situ* samples taken at different points along the first electrochemical cycle, and a thorough study of the effects of desodiation upon the magnetism of the Na_xMnO_2 lattice, will be the subject of a future publication.

While the collapse of long-range order on Na extraction inhibits a detailed understanding of the structure of the Na deficient materials it is apparent that the structural changes observed when Na is extracted are reversed when Na is subsequently electrochemically reinserted in the cathode material. PXRD, which probes long-range order, together with NMR and HRTEM, which probe short-range order, demonstrate the reversibility of the structure over both length scales. Indeed, the powder X-ray diffraction patterns during the Na reinsertion process mirror those acquired when Na is extracted. A composition of β - $\text{Na}_{0.92}\text{MnO}_2$, based on the charge passed during the cycle and confirmed by ICP ($\text{Na}_{0.89}\text{MnO}_2$), is obtained at the end of the first discharge. The NMR data are also consistent with a high degree of reversibility, with the spectrum obtained at the end of the first discharge comparable to the one obtained on the pristine material. The TEM data acquired at the end of discharge (Figure S2 c) show that the domain structure formed when Na is extracted is retained, however structural order is also restored, in good accord with the PXRD and NMR data.

PXRD, TEM and NMR data collected after 5 full Na extraction/reinsertion cycles, Figures 3, S2 d) and S3, show that the material exhibits a larger proportion of stacking faults after 5 cycles and an increased amount of local regions of α -like Na layer stacking.

Our analysis of the changes in the structure of the cathode material upon cycling indicates that β - NaMnO_2 has a complex intergrowth structure and that the long range order present in the as-prepared material collapses when Na is extracted, and is then recovered when Na is reinserted, but with an increase in the proportion of twin boundaries. Despite these changes the electrochemistry is

very stable on cycling, as shown in Figure 2. This is in contrast to the common expectation that stable and reproducible load curves require minimal structural changes. We interpret the relative insensitivity of the electrochemistry to the number of twin boundaries as reflecting the similarity in the energies of the α and β structure types.³⁵ Such similarities imply that the energetics of Na removal, whether from α , β or the twin boundaries is similar and dependent primarily on the local structure around Na^+ and the electrons ($\text{Mn}^{4+/3+}$). Although a small polarization (150 mV) is observed along the 2.7 V plateau, the polarization reached a value of 600 mV below $x = 0.4$. The large cell polarization at low Na content may result from the collapse of the long range structure. Changes in the structure at short length scales are also observed at low Na content ($x < 0.4$). The broadening of the Na resonances in the NMR spectrum of the $\text{Na}_{0.236}\text{MnO}_2$ sample indicates the formation of a range of Na local environments. The restoration of long range order and of the structure at short length scales as Na is reinserted, and the stability of the load curve on cycling, indicate that the processes occurring when $x < 0.4$ are fully reversible.

3.3. Cycling rate and stability

The rate performance of $\beta\text{-NaMnO}_2$ is shown in Figure 6.

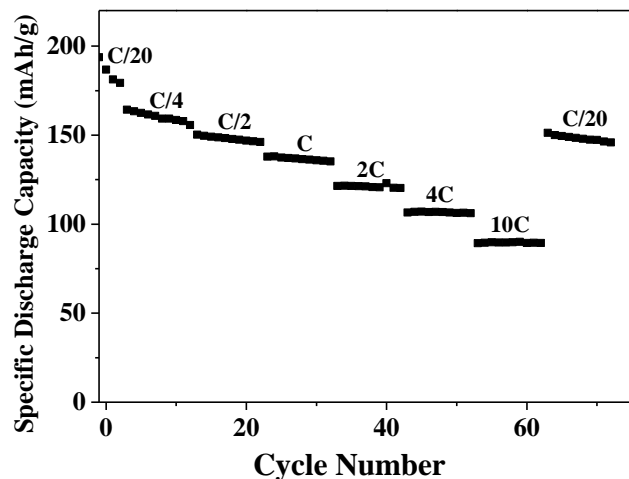


Figure 6. Cycling data for $\beta\text{-NaMnO}_2$ obtained between 2 and 4.2 V vs. Na^+/Na at various rates and at room temperature. The data were recorded for a single cell, and the applied current was varied every 10 cycles. The Na extraction process was performed at a rate of C/4, and the Na reinsertion process at a rate indicated on top of each set of data, except for the data acquired at a rate of C/20, for which Na extraction was also performed at a rate of C/20.

The first cycles are carried out at a charge and discharge rate of C/20 (that is, a rate of C/20 for both Na extraction and reinsertion processes), while subsequent cycles involved charging the cell at a C/4 rate and discharging the cell at increasing C-rates, as indicated in Figure 6. At C/2, a capacity of 150 mA h g^{-1} is obtained, which drops to 90 mA h g^{-1} at 10 C. When the discharge

rate is reduced to C/20 a capacity of 152 mA h g^{-1} is recovered. Clearly, there is an irreversible loss of capacity on cycling, as the capacity does not return to its initial value. In order to explore the cyclability of the material in more detail, continuous cycling at a range of rates was carried out, and is presented in Figure 7.

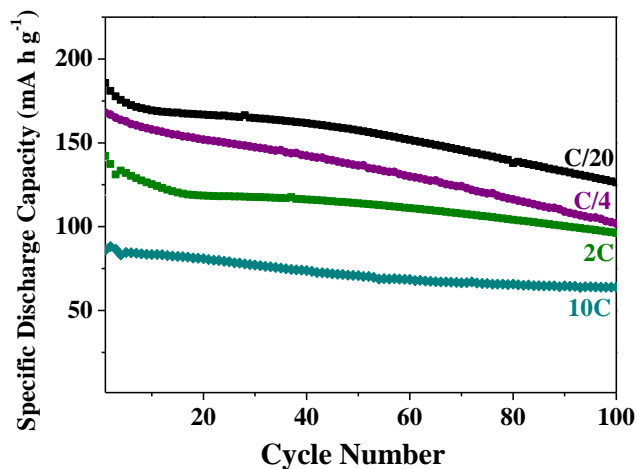


Figure 7. Values of specific discharge capacities for $\beta\text{-NaMnO}_2$ cycled between 2 and 4.2 V vs. Na^+/Na at room temperature. 100 cycles are presented for each rate (from C/20 to 10C). The Na extraction process was performed at a rate of C/4, and the Na reinsertion process at a rate indicated on top of each set of data, except for the data acquired at a rate of C/20, for which Na extraction was also performed at a rate of C/20. Black squares correspond to a rate of C/20, purple squares to C/4, green squares to C/4 and blue squares to 10C.

Except for the data acquired at C/20, the rest of the cycling data were collected with a charge rate of C/4 and with discharge rates indicated in Figure 7. The data obtained upon cycling the cell at equal charge and discharge rates are shown in Figure S5. A comparison of the two sets of data indicates that the kinetics of the Na extraction process are relatively slow, and that the Na extraction capacity decreases markedly with increasing Na extraction rate. Although the capacity is reduced at higher cycling rates, the capacity retention improves. As noted previously, capacity fading at low rates is associated mainly with the voltage plateau at 2.6 V. The load curves obtained at both low and high rates (C/20 and 10C) for cycle number 5 in Figure S6 demonstrate that there is little contribution from the plateau region at these rates, consistent with the fact that the capacity does not fade. The reason the plateau region is not traversed at high rates is that it is associated with a kinetically slow two-phase process with significantly different lattice parameters between the Jahn-Teller distorted and undistorted phases. This can be seen in the GITT plot presented in Figure S6, where significant polarization is apparent during Na insertion, along the plateau. It should also be recalled that Mn^{3+} containing electrodes are prone to some degree of Mn^{2+} dissolution in the electrolyte, something that will be

more prominent near full Na insertion where the concentration of Mn^{3+} is greatest.

CONCLUSIONS

β - NaMnO_2 has been prepared, characterized using a range of techniques including PXRD, HRTEM and ^{23}Na NMR, and its behavior as a cathode material in sodium-ion batteries studied. ^{23}Na NMR reveals the presence of Na sites intermediate between the two Na environments present in the ideal α and β polymorphs, assigned to Na sites in the vicinity of a planar defect between the two polymorphic forms. The high fraction of Na atoms in these intermediate sites indicates a high propensity for the formation of planar defects in β - NaMnO_2 , in agreement with the Diffax simulations of the XRD data.

This compound exhibits a high discharge capacity of 190 mA h g^{-1} at low rate of C/20 when tested as a cathode in sodium-ion batteries. The compound also shows good rate capability with 142 mA h g^{-1} at 2C and 90 mA h g^{-1} at a rate of 10C.

The complex structural changes occurring upon cycling have been monitored and characterized using *in situ* XRD, ^{23}Na NMR and HRTEM, showing that the proportion of stacking faults increases upon Na extraction, associated with a loss of crystallinity. Upon Na reinsertion however, the structure is recovered, although exhibiting increased disorder. In view of the severe order/disorder changes that accompany cycling, the reversibility of the transformation, and associated reproducibility of the load curve is remarkable, as is the rate capability of the electrode. It is in contrast with common expectation that stable reproducible cycling requires minimal structural change between the structures with highest and lowest Na content, that is, the charged and discharged states.

ASSOCIATED CONTENT

Supporting Information. Simulations using Diffax, HRTEM images of the pristine sample, the sample at the end of the first charge, the sample at the end of the first discharge, and after 5 cycles, ^{23}Na NMR of the β polymorph after 5 cycles and α polymorph, load curves at various rates and GITT.

AUTHOR INFORMATION

Corresponding Author

* Email: peter.bruce@materials.ox.ac.uk

Author Contributions

The manuscript was written through contributions of all authors. All authors have given approval to the final version of the manuscript.

ACKNOWLEDGMENT

We thank Ieuan Seymour for the synthesis of the α - NaMnO_2 polymorph, and for helpful discussion. We would also like to thank Dr. Michal Leskes and Dr. Phoebe Allan for helpful discussion and suggestions. RJC acknowledges support from the European Research Council (ERC). PGB acknowledges

support from EPSRC including the SUPERGEN programme. JCV is grateful to MAT2010-19837-Co6-Co4 for funding.

REFERENCES

- (1) S-W. Kim, D-H Seo, X. Ma, G. Ceder and K. Kang, *Adv. Energy Mater.*, **2012**, 2, 710
- (2) B. L. Ellis and L. F. Nazar, *Current Opinion in Solid State and Materials Science*, **2012**, 16, 168.
- (3) a) V. Palomares, P. Serras, I. Villaluenga, K. B. Hueso, J. C. González, and T. Rojo, *Energy Environ. Sci.*, **2012**, 5, 5884; b) V. Palomares, M. C. Cabanas, E. C. Martínez, M. H. Han and T. Rojo, *Energy Environ. Sci.*, **2013**, 6, 2312; c) C. Masquelier and L. Croguennec, *Chem. Rev.*, **2013**, 113, 6552.
- (4) H. Pan, Y.-S. Hu and L. Chen, *Energy Environ. Sci.*, **2013**, 6, 2338
- (5) M. D. Slater, D. Kim, E. Lee, C. S. Johnson, *Adv. Funct. Mater.*, **2013**, 23, 947
- (6) A. Ponrouch, E. Marchante, M. Courty, J.-M. Tarascon and M. R. Palacin, *Energy Environ. Sci.*, **2012**, 5, 8572
- (7) S. Y. Lim, H. Kim, R. A. Shakoor, Y. Jung and J. W. Choi, *J. Electrochem. Soc.*, **2012**, 159, A1393.
- (8) Z. Jian, W. Han, X. Lu, H. Yang, Y.-S. Hu, J. Zhou, Z. Zhou, J. Li, W. Chen, D. Chen and L. Chen, *Adv. Energy Mater.*, **2013**, 3, 156.
- (9) J. Kang, S. Baek, V. Mathew, J. Gim, J. Song, H. Park, E. Chae, A. K. Rai and J. Kim, *J. Mater. Chem.*, **2012**, 22, 20857.
- (10) K. Saravannan, C. W. Mason, A. Rudola, K. H. Wong and P. Balaya, *Adv. Energy Mater.*, **2013**, 3, 444.
- (11) T. Nagura and K. Tozawa, *Prog. Batt. Solar Cells*, **1990**, 9, 209.
- (12) Z. Lu, D. D. MacNeil and J. R. Dahn, *Electrochem. Solid State Lett.*, **2001**, 4, 191.
- (13) T. Ohzuku and Y. Makimura, *Chem. Lett.*, **2001**, 642, 744.
- (14) E. Rosen, C. D.W. Jones and J. R. Dahn, *Solid State Ionics*, **1992**, 57, 311.
- (15) M. E. Spahr, P. Novak, B. Schnyder, O. Haas and R. Nesper, *J. Electrochem. Soc.*, **1998**, 145, 1113.
- (16) D. D. MacNeil, Z. Lu and J. R. Dahn, *J. Electrochem. Soc.*, **2002**, 149, A1332.
- (17) N. Yabuuchi, H. Yoshida and S. Komaba, *Electrochemistry*, **2012**, 80, 716.
- (18) S. Komaba, C. Takei, T. Nakayama, A. Ogata and N. Yabuuchi, *Electrochem. Commun.*, **2010**, 12, 355.
- (19) X. Ma, H. Chen and G. Ceder, *J. Electrochem. Soc.*, **2011**, 158, A1307.
- (20) a) A. R. Armstrong and P. G. Bruce, *Nature*, **1996**, 381, 499; b) F. Capitaine, P. Gravereau, and C. Delmas, *Solid State Ionics*, **1996**, 89, 197; c) M. M. Doeff, M. Y. Peng, Y. Ma and L. C. De Jonghe, *J. Electrochem. Soc.*, **1994**, 11, L146
- (21) A. R. Armstrong, N. Dupre, A. J. Paterson, C. P. Grey and P. G. Bruce, *Chem. Mater.*, **2004**, 16, 3106.
- (22) A. Mendiboure, C. Delmas and P. Hagenmuller, *J. Solid State Chem.*, **1985**, 57, 323.
- (23) A. Caballero, L. Hernan, J. Morales, L. Sanchez, J. Santos Pena and M. A. G. Aranda, *J. Mater. Chem.*, **2002**, 12, 1142.
- (24) D. Su, C. Wang, H.-J. Ahn and G. Wang, *Chem. Eur. Journal*, **2013**, 19, 10884.
- (25) J. Billaud, G. Singh, A. R. Armstrong, E. Gonzalo, V. Roddatis, M. Armand, T. Rojo and P. G. Bruce, *Energy Environ. Sci.*, **2014**, 7, 1387.
- (26) N. Yabuuchi, R. Hara, M. Kajiyama, K. Kubota, T. Ishigaki, A. Hoshikawa and S. Komaba, *Adv. Energy Mater.*, **2014**, 4, 1301453.
- (27) J. Xu, D. H. Lee, R. J. Clément, X. Yu, M. Leskes, A. J. Pell, G. Pintacuda, X.-Q. Yang, C. P. Grey and Y. S. Meng, *Chem. Mater.*, **2014**, 26, 1260.

- (28) N. Yabuuchi, M. Kajiyama, J. Iwatate, H. Nishikawa, S. Hitomi, R. Okuyama, R. Usui, Y. Yamada and S. Komaba, *Nature Mater.*, **2012**, 11 512.
- (29) B. Mortemard de Boisse, D. Carlier, M. Guignard, and C. Delmas, *J. Electrochem. Soc.*, **2013**, 160, A569.
- (30) C. Delmas, C. Fouassier, and P. Hagenmuller, *Physica B+C*, **1980**, 99, 81.
- (31) J.P. Parant, R. Olazcuaga, M. Devalette, C. Fouassier and P. Hagenmuller, *J. Solid State Chem.*, **1971**, 3, 1
- (32) M. M. Treacy, M. W. Deem and J. M. Newsam, *Diffax*, V1.76, 1990.
- (33) C. Tessier, P. H. Haumesser, P. Bernard and C. Delmas, *J. Electrochem. Soc.*, **1999**, 146,6
- (34) Y. Chabre and J. Pannetier, *Prog. Solid St. Chem.* **23**, **1995**
- (35) L. Croguennec, P. Deniard, R. Brec and A. Lecerf, *J. Mater. Chem.*, **1997**, 7, 511
- (36) A. M. Abakumov, A. A. Tsirlin, I. Bakaimi, G. Van Tendeloo and A. Lappas, *Chem. Mater.*, **2014**, 26, 3306
- (37) K. A. Aldi, A solid state NMR and EXAFS study of manganese oxide minerals [dissertation]. Ann Arbor: State University of New York at Stony Brook; 2011.

Graphical abstract:

